Toward 5G/mm-Wave Shape-Changing Origami-Inspired Phased Arrays for Near-Limitless Arbitrarily Reconfigurable Radiation Patterns: Realization, Actuation, and Calibration

Hani Al Jamal, *Graduate Student Member, IEEE*, Chenhao Hu, *Graduate Student Member, IEEE*, Edward Kwao, *Graduate Student Member, IEEE*, Kai Zeng, *Member, IEEE*, and Manos M. Tentzeris, *Fellow, IEEE*

***Abstract*— This article presents the first shape-changing phased array operating at 28 GHz as an alternative to traditional planar phased arrays. By combining electrical beamsteering with mechanical shape change, this design achieves high degrees of freedom, resulting in near-limitless radiation pattern reconfigurability and overcoming the tradeoff between gain and angular coverage. Utilizing the eggbox origami structure, a 4-D multifaceted foldable phased array is developed, and a modular tile-based (unit-cell) approach is employed to enable TX/RX selective activation and scalability to massive MIMO. This results in near 360° continuous beam steering in the azimuth plane with reconfigurable multibeam or quasi-isotropic radiation patterns. Additive manufacturing processes are employed to realize the first shape-changing phased array at a miniaturized millimeter scale. The eggbox phased array features highly integrated on-structure beamformer ICs and a flexible feeding network utilizing a uniquely designed foldable interconnect. As the first additively manufactured mm-wave hinge interconnects, the presented "arch" interconnect exhibits near-constant insertion loss of 0.02 dB/mm across various folding angles and cycles. In addition, a microservo-based actuation mechanism is designed to precisely control the origami folding action. Measurements demonstrate the phased array's pattern reconfigurability, and its effectiveness is further validated in an orthogonal frequency division multiplexing (OFDM)-based communication testbed setup. Furthermore, this article provides a holistic multidisciplinary framework guiding the development of a new era of mm-wave shape-changing phased arrays, encompassing considerations in hardware realization, actuation, and 3-D beam shaping/calibration. Given its multitude of novel features, the eggbox phased array can enable a plethora of applications, ranging from multimode in-band full-duplex applications to multifunction multibeam use cases, extreme interference mitigation, and space-constrained deployments.**

***Index Terms*— 5G, additive manufacturing, beamformer IC, mm-wave, origami, origami actuation, phased array.**

Received 8 July 2024; revised 6 September 2024 and 12 September 2024; accepted 15 September 2024. Date of publication 1 October 2024; date of current version 7 January 2025. This work was supported in part by the Office of the Under Secretary of Defense, Research and Engineering (OUSD, R&E) through the Naval Information Warfare Center, Atlantic under Contract N6523622C8018. *(Corresponding author: Hani Al Jamal.)*

Hani Al Jamal, Chenhao Hu, and Manos M. Tentzeris are with the School of Electrical and Computer Engineering, Georgia Institute of Technology, Atlanta, GA 30332 USA (e-mail: hani.aljamal@ieee.org).

Edward Kwao and Kai Zeng are with the Department of Electrical and Computer Engineering, Cyber Security Engineering, and the Department of Computer Science, George Mason University, Fairfax, VA 22030 USA.

Color versions of one or more figures in this article are available at https://doi.org/10.1109/TMTT.2024.3463484.

Digital Object Identifier 10.1109/TMTT.2024.3463484

I. Introduction

THE advent of 5G mm-wave technology has revolutionized the landscape of high-speed communications. This advancement unlocked unprecedented potential for the development of smart cities, Industry 4.0, and consumer-focused IoT through broadband, high data rate, and ultrareliable low-latency communication. Nevertheless, the realization of the full potential of 5G mm-wave applications faces significant challenges. One primary issue is the effectiveness of mm-wave signals, which experience considerable deterioration in non-line-of-sight conditions due to the high path loss incurred.

The utilization of phased arrays has become imperative to 5G deployment, offering beamsteering capabilities that can reduce interference by directly targeting users. However, conventional phased arrays struggle with inherent limitations, primarily their restricted angular coverage and narrow beamwidths. Moreover, the bulkiness, cost, and rigidity of these systems hinder adaptability, making modification or replacement of subsystem components a daunting task.

Recognizing the constraints of planar phased arrays, reconfigurability methods for antennas as a means to enhance their performance are explored. Reconfigurable antenna characteristics include frequency, radiation pattern, polarization, aperture size, field of view, gain, and sidelobe levels (SLL). Several methods exist to achieve this reconfigurability, with the most prominent being switch-based techniques that utilize electronic switches such as p-i-n diodes or varactors [1]. On the other hand, nonswitch-based reconfiguration techniques alter the antenna's characteristics without resorting to switching components by modifying the shape of the antenna or introducing deformations in its substrate and/or ground plane.

Origami, the Japanese art of paper-folding, emerges as a vehicle to enable shape-changing antennas. Origami antennas, spanning diverse materials such as paper [2], PET [3], and 3-D-printed structures [4], have demonstrated frequency reconfigurability up to 4.45 GHz. For instance, [5] presents

an origami helical antenna capable of changing its resonant frequency in the 0.86–3-GHz band. Similarly, [6] showcases a 1–5-GHz frequency reconfigurable antenna based on a tristable square-twist origami structure.

Reconfigurability in antenna radiation pattern due to shape change has been less prominent in the literature but has been presented at 2.2 GHz using a quasi-Yagi helical antenna [3]. A two-state pattern and frequency reconfigurable antenna based on Nojima origami is presented in [7], while another two-state pattern reconfigurable antenna operating at 2.4 GHz based on folding techniques is demonstrated in [8]. A thorough review of origami antennas can be found in [9], [10], and [11].

Shape-changing origami-inspired *antenna arrays* have not been extensively explored, with few demonstrations in the literature. For example, [12] presents an accordion-folding series-fed patch array for deployable applications with minimal frequency shifts at 5.7 GHz. This array, however, still requires an external feeding network. In contrast, [13] investigates a four-element patch array based on thick-origami principles with an on-structure feeding network, with the capability to perform limited beamsteering at 2.45 GHz through shape change. Similarly, [14] investigates a Miura-Ori origami antenna array featuring up to four patch elements at 3 GHz, also with an on-structure feeding network, posing higher integration levels. However, challenges surfaced as connecting interconnects extended over folds, impacting performance with changing folding angles.

Notably, the aforementioned arrays lacked the wide angular-coverage beamsteering capabilities inherent in phased arrays, behaving more akin to a single antenna. This drove Williams et al. [15] to develop an origami-inspired *phased array* at 2.6 GHz, boasting an array of 3×5 elements. While demonstrating the ability to morph into planar, cylindrical, and circular geometries, this structure encounters limitations in terms of size, bulkiness, and scalability, posing challenges to its practical implementation. Designed for 2.6-GHz operation, the work in [15] is not suitable for mm-wave applications, is not additively manufactured, and does not present foldable hinge interconnects for higher integration levels and scalability.

The recent introduction of shape-changing phased arrays presents a new paradigm shift in antenna reconfigurability. The combination of electrical beamsteering and mechanical shape change leads to additional degrees of freedom and, thus, reconfigurability. In fact, a radiator capable of arbitrarily controlling both its geometry and the current distribution on its surface would have no constraints on the radiation patterns that it could produce. Such shape-changing phased arrays enable new applications by dynamically conforming their shapes to the geometry best suited for a given task.

To the best of our knowledge, this article presents the first morphing origami-inspired phased array enabling near-limitless radiation pattern reconfigurability at 28 GHz. In addition, operating at mm-wave frequencies renders the proposed phased array to be the first origami-inspired phased array realized at this scale (maximum volume of 6.36 cm^3 per unit cell), presenting unique fabrication challenges tackled by the authors. The proposed shape-changing phased array employs the eggbox origami structure, foldable along two planes, multifaceted, and enabling a unit-cell approach to be utilized, as shown in Fig. 1. Each unit cell incorporates the antenna elements, a face-to-face feeding network, and four on-structure beamformer ICs.

The proposed work therein presents several novelties. First, the combination of mechanical and electrical reconfigurability enables continuous 360° beamsteering through 2 degrees of freedom (2-DOF) resulting in virtually infinite radiation pattern reconfigurability capabilities. Second, the multifaceted 3-D nature of the phased array leads to highly reconfigurable multibeam directional or quasi-isotropic patterns. Third, the proposed origami-inspired phased array is fully contained with on-structure beamforming RFICs and a flexible feeding network that utilizes the first additively manufactured foldable hinge interconnect ("arch" interconnect) exhibiting near-constant insertion loss across folding angles and cycles. The result of this is a lightweight prototype with a small form factor. Fourth, a modular tile-based approach is employed; realizing the proposed eggbox origami phased array through scalable unit cells. This not only allows for scalability but also reduces costs in case of failure, as unit cells can be individually replaced. In addition, a modular tile-based approach allows for the selective activation of specific unit cells of eggbox faces based on desired patterns, TX/RX modes, and/or power consumption requirements. Finally, the use of additive manufacturing techniques leads to reduced waste, faster fabrication, and lower costs.

The eggbox phased array offers versatile application scenarios across various domains. First, it enables multimode in-band full-duplex applications by selectively or simultaneously activating different faces or unit cells as transmitters (TX) or receivers (RX). This capability allows the array to function as an active transmit–receive relay system, where a signal is received from one side and transmitted in another direction, enhancing communication efficiency and reliability. Second, its multifunctionality is exemplified by its multibeam capability, which is invaluable for autonomous vehicles. Different beams can be allocated for specific tasks such as communication, obstacle detection, and navigation or in military applications where beams are used for jamming, radar, and communication, ensuring comprehensive situational awareness and operational effectiveness. Third, the eggbox phased array can be deployed in search and rescue operations, particularly when mounted on an aircraft. Its geometric configuration addresses the tradeoff between gain and angular coverage; when unfolded, it provides wide angular coverage for rapid search operations and can then be folded to offer narrow beams with high gain for precise localization. Finally, its ability to be easily folded and deployed is crucial for space-constrained environments, such as space applications, where compactness and efficient deployment are essential. This adaptability presents the eggbox phased array as versatile and impactful with broad applicability.

This article extends our previous work [16] with several new contributions. First, we discuss the implications and effects of shape change on antenna arrays in Section II-A, followed by an overview of the practical aspects involved in the holistic

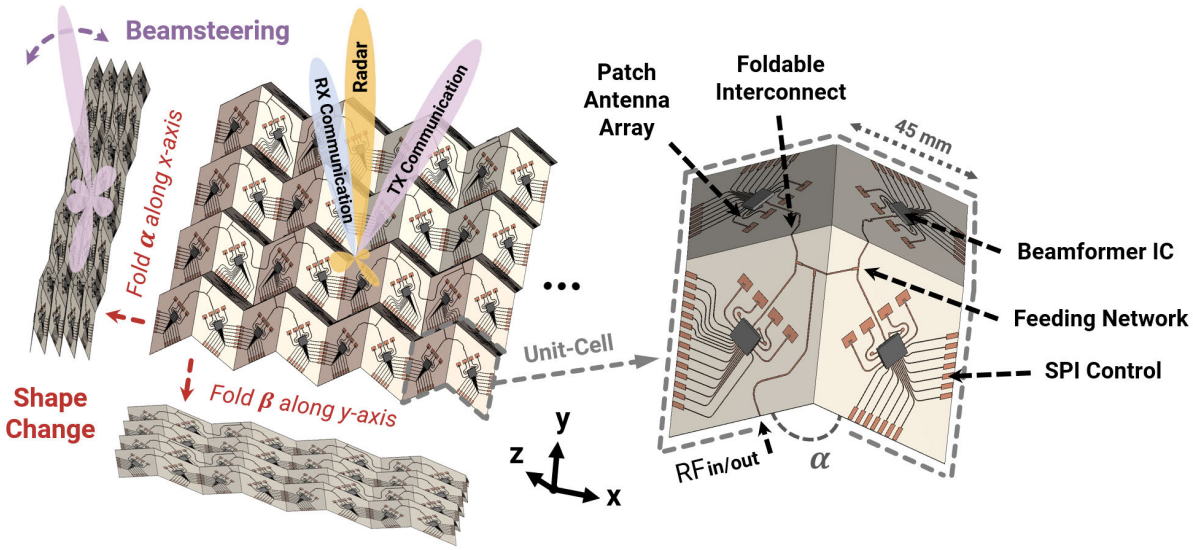

Fig. 1. Conceptual illustration of an $n \times n$ origami-inspired eggbox antenna array with 2-DOF electrical beamsteering and mechanical shape change. Each eggbox unit-cell face can be selectively activated in transmit or receive mode. A single unit cell is highlighted ($\alpha = 90°$), with a geometrically optimized face-to-face feeding network and integration of four BFICs.

implementation of a shape-changing phased array, including hardware realization, mechanical actuation, and electrical calibration, as detailed in Section II-B. The folding action of the proposed eggbox origami structure is mathematically outlined in Section III-A, with the design and simulation results of the 16- and 64-element eggbox phased arrays demonstrating multibeam radiation pattern reconfigurability, as presented in Section III-B. The additive manufacturing fabrication process is further detailed in Sections IV-A and IV-B, followed by the introduction of the umbrella-inspired microservo-based actuation mechanism, presented for the first time in Section IV-C. Finally, we report measurements illustrating pattern reconfigurability due to mechanical shape change and electrical beamsteering in Section V, followed by a system-level orthogonal frequency-division multiplexing (OFDM)-based communication testbed setup in Section V-B, which demonstrates the validity and capability of additive manufacturing in realizing functional prototypes with high levels of technology readiness. These additions provide a comprehensive extension and holistic analysis of our previous work [16]. As will become apparent throughout this article, the successful realization of a shape-changing phased array requires a multidisciplinary approach, leveraging structural engineering, materials, mechanics, and calibration techniques, with electromagnetics playing a central role in orchestrating and guiding the integration of these efforts.

II. Overview

A. Implications of Shape Change on Antenna Arrays

Shape-changing antennas can be seen as an extension of conformal antennas, first introduced in 1987 [17]. Initially, conformal antennas were defined as being mounted on flexible and/or stretchable sheets. However, this concept can be extended to shape-changing arrays that are multifaceted, where the art of origami presents itself as a naturally elegant choice for folding complex structures. These dynamically shape-changing arrays can morph into different geometries, unlike traditional conformal arrays that consist of a single flexible sheet.

Traditional phased arrays, while versatile, are limited by their fixed geometries, which constrain the achievable radiation patterns, maximum gain, and steering range due to the fixed element orientation and interelement spacing. Shape-changing phased arrays, particularly those employing origami principles, can overcome these limitations by dynamically altering their geometrical configuration, which allows for intentional changes in antenna properties. As the array's shape changes, the relative positions and orientations of its elements also change, effectively transforming it into a new array. This results in changes in coupling and ground plane deformation, which alter port impedances and individual element patterns, and changes in orientation, which disrupt the overall array pattern imposed by the element pattern. Consequently, the interference pattern of the radiation is altered in both near and far fields [18]. Moreover, transmission line propagation characteristics change when bent or folded.

Shape change also fundamentally alters the array's aperture size, thereby affecting its maximum gain and steering range. In fact, while there exists a tradeoff between maximum gain and steering range, shape change can be employed to break this tradeoff. This idea is further studied in [19] for spherical, conical, and cylindrical phased arrays and for multifaceted geometries in [17].

A planar phased array antenna typically cannot steer its beam more than about 60° from the normal due to beam broadening, mutual coupling, and impedance variations, which lead to gain reduction. However, multifaceted phased arrays capable of reconfiguring their shape offer a shape-controlled gain that does not drop with scan angles, providing wider angular coverage and near-limitless radiation patterns when strategically combined with selective beamforming. Electrical beamforming also improves the phased array's performance by compensating for the fact that only one geometric configuration can ideally achieve a $\lambda/2$ spacing between its elements.

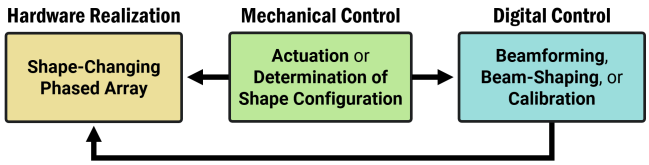

Fig. 2. Practical realization of a shape-changing phased array antenna requires the implementation of three interdependent efforts.

In summary, although shape-changing origami antennas have been explored in the literature as aforementioned, combining electrical beamsteering with shape change unlocks unprecedented capabilities that remain largely uncharted.

B. Implementation of Shape-Changing Phased Arrays

A successful practical implementation of a shape-changing phased array antenna necessitates the confluence of three interdependent efforts: hardware realization (fabrication), a method for mechanical control if shape change is utilized intentionally or a technique for determining the geometrical configuration if an uncontrolled external stimulus affects the shape, and a digital control scheme for beam shaping and/or electronic calibration. The relationship between the three efforts is illustrated in Fig. 2.

1) Hardware Realization: The physical realization of a shape-changing phased array requires a comprehensive understanding of applicable materials, design principles, and fabrication processes. While paper [2], [20] and flexible PET [3] have been extensively used to create origami antennas, phased arrays require the incorporation of active integrated circuits and structural rigidity. In addition, unlike most origami antennas in the literature that are manually actuated, we advocate for the use of programmable actuation mechanisms to enable practical application scenarios, as will be discussed in Section II-B2. The chosen actuation mechanism will also influence the selection of materials.

Furthermore, when connecting antennas and RF circuitry on different facets of the origami structure through transmission lines, special attention must be given to the mechanical distortion that these lines undergo during shape changes. The folding interconnects must be flexible and mechanically reliable to handle the sharp bends required for folding. Any instability in electrical performance due to folding should be accounted for or intentionally utilized to introduce controllable frequency and/or pattern reconfigurability. This discussion pertains to highly integrated shape-changing phased arrays, where the radiators, phase shifters, amplifiers, digital circuitry, and feeding networks are integrated on the shape-changing array.

Shape-changing arrays can also be categorized based on their mechanical backbone structure: those where the dielectric substrate itself forms the backbone and to which conductors are directly printed onto it [13] and [14] or those using a separate mechanical structure to create the origami tessellations, with a flexible or rigid substrate attached to the facets of the backbone structure [15], [21]. Given these considerations, various fabrication techniques are available. For fully contained and lightweight shape-changing phased arrays, however, additive manufacturing techniques are particularly promising as they allow for customized, on-demand fabrication of complex geometries, integration of diverse materials in a single manufacturing process, and support rapid prototyping.

In addition to the aforementioned considerations, thermal management is a crucial factor when integrating active components, such as beamformer ICs, onto foldable and thin dielectric materials used in shape-changing phased arrays. While the use of thermal via arrays has been adequate for managing heat dissipation during short- to medium-duration testing scenarios, as demonstrated in this work, more advanced thermal management solutions will be required as the technology matures. The flexibility offered by additive manufacturing processes allows for the integration of heat-dissipating materials or even microfluidic-based cooling channels directly into the flexible substrate beneath the beamformer ICs, as demonstrated in [22].

2) Mechanical Control: The actuation of origami, or more generally, conformal antenna arrays, falls under two main categories: intentional actuation utilizing a controlled actuation mechanism or uncontrolled in situ actuation where an external stimulus acts on the antenna array, changing its shape. To intentionally reconfigure the antenna characteristics through folding and unfolding, the origami array can be actuated using a multitude of ways. The feasibility and choice of the actuation mechanism highly depend on the origami shape and materials utilized. Most commonly, manual actuation (which cannot be controlled) is employed, as is the case in most references on origami antennas, unless otherwise noted.

Actuation mechanisms include manual actuation using cables [15], motor-driven mechanisms [23], pneumatic actuators that use air pressure to inflate, deflate, or deploy structures [24], [25], and hydraulic actuators that fold origami structures using liquid hydrogels [26] or microfluidic channels [27]. These methods utilize mechanical loads to actuate the origami structure. Alternatively, active materials that reconfigure in shape in response to stimuli can be utilized. This includes shape memory alloys (SMAs), smart flexible materials controlled using a direct current [28], or SMA springs as electromechanical actuators [29]. Shape memory polymer (SMP) hinges can also be employed, which deforms upon heating [30], [31], [32] or exposure to other external stimuli such as light [33] or humidity [34]. Thermal actuation can be achieved through multimaterial origami [35], [36], and magnetic actuation provides noncontact actuation through an externally applied magnetic field [37], [38] or using magnetic soft materials (MSMs) [39]. Finally, 4-D printing can be used, which allows for self-actuation as demonstrated by Kimionis et al. [40].

On the other hand, if the array is deformed through an external force, a method for knowing and reconstructing the shape must be used to subsequently perform beam shaping or to calibrate the array. This includes the use of flexible external resistive sensors [41], [42], the array's mutual coupling [43], or, more recently, computer vision techniques [44].

3) Digital Control: While the analysis of a shape-changing phased array for a given shape and beamforming configuration is a mathematically tedious but straightforward task, the synthesis of a desired pattern poses a more challenging,

nonlinear problem with no unique solution. That is, while the power of shape-changing phased arrays lies in their ability to generate near-limitless patterns, the synthesis problem of these patterns is rather complex. Moreover, while synthesis techniques for linear arrays can be extended to planar antennas, these methods cannot be directly carried over to conformal or 3-D phased arrays or, more specifically, dynamically shape-changing phased arrays, presenting a unique challenge.

To synthesize patterns for 3-D phased arrays, several methods exist, including the aperture projection method [19], alternating projections [45], iterative least-mean-squares [46], and polarimetric synthesis [47]. Optimization algorithms, such as simulated annealing and genetic algorithms, are also used, often integrated into commercial 3-D electromagnetic simulation tools, as reviewed in [17].

Alternatively, calibration methods can be employed to find the optimal beamforming configuration for a given antenna geometry and for a desired pattern. For simple geometries, calibration equations are effective [44]. Other approaches include open-circuit [48], Huang's algorithm [49], and mutual-coupling calibration [50]. More recent methods, such as blind beamforming based on cumulant analysis [51], remain theoretical and have yet to be applied to shape-changing phased arrays.

Given the complexity of shape-changing structures, in situ synthesis/calibration is often impractical due to high computational demands. Presynthesized codebooks may be more efficient, particularly with the potential integration of machine learning algorithms to predict suitable element excitations. Although machine learning has not yet been explored for pattern calibration in shape-changing origami-inspired phased arrays to the best of our knowledge, it offers promising opportunities for future development.

4) This Work: The proposed work introduces several novelties in the design of shape-changing, origami-inspired phased arrays. It is the first to integrate active integrated circuits directly onto the shape-changing structure itself. Moreover, being the first shape-changing phased array of this scale, it includes the first additively manufactured, reliably foldable interconnect to connect different facets of the eggbox origami structure, resulting in a fully contained and compact design. Utilizing additive manufacturing techniques such as inkjet and 3-D printing, a flexible 3-D printed structure serves as the mechanical backbone, onto which a flexible substrate encompassing the radiators, beamformer ICs, and feeding network is attached. In addition, a proof-of-concept microservo-based actuation mechanism is designed to electronically actuate the origami eggbox structure. Finally, beam shaping and calibration are performed based on a presynthesized codebook containing strategic configurations selected through an analysis of the dynamic morphology of the eggbox structure.

III. Design and Simulation

A comprehensive design and simulation processes of the proposed eggbox phased array are presented. Section III-A discusses the mathematical formulation and mechanical design of the eggbox origami shape. Section III-B then presents the design and simulation of both a single unit cell and a 2×2 unit-cell eggbox phased array, showcasing its modes of operation, capabilities, and electrical/mechanical reconfigurability.

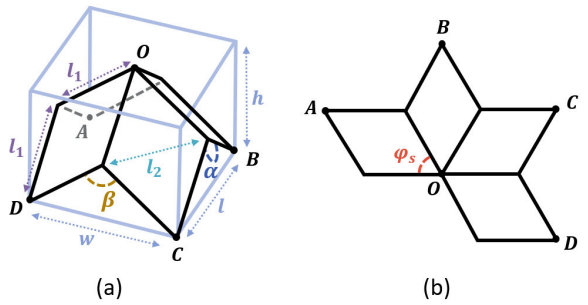

Fig. 3. Eggbox origami unit-cell design: (a) 3-D structure in the unfolded state and (b) planar outline.

A. Eggbox Origami Unit-Cell Design

The eggbox origami is a bidirectional symmetric and nondevelopable pyramidal truss structure, where the orientation of the pyramids alternates in a chequerboard-like fashion [see Fig. 1(a)]. It features additional degrees of reconfigurability compared to the widely used Miura-Ori origami, as it has the ability to compress in two orthogonal directions [52]. This increased flexibility, combined with its simpler fabrication using flexible 3-D printed materials compared to more complex tessellations, such as the waterbomb origami tessellation, made the eggbox the optimal choice for this application.

An eggbox origami unit cell is shown in Fig. 3(a) and can be defined by two lengths, l_1 and l_2. When the eggbox is in its natural unfolded state, the fold angles α and β will be equal and given by

$$\alpha = \beta = 2 \times \arccos\left(\sqrt{\left(1 - \frac{l_2^2}{2l_1^2}\right)}\right). \tag{1}$$

In this work, $l_1 = l_2 = 45$ mm was chosen to accommodate the printed antenna elements and ensure good foldability. As such, $\alpha = \beta = 90°$ (unfolded). When folded, the mathematical relationship between α and β is discussed in [53]. A volumetric boundary box of an eggbox unit cell is given by the dimensions w, l, and h, respectively, calculated by

$$w = 2\, l_1 \sin(0.5\beta) \tag{2}$$

$$l = 2\, l_1 \sin(0.5\alpha) \tag{3}$$

$$h = l_1 \cos(0.5\alpha) + l_1 \cos(0.5\beta). \tag{4}$$

As will be apparent in Section III-B, it is convenient to utilize a planar mapped projection of the 3-D eggbox origami. Given that the eggbox is a nondevelopable origami structure, it cannot be unfolded into a flat sheet without stretching or cutting. Therefore, a cut along one of the four eggbox faces allows for a planar structure of the eggbox [see Fig. 3(b)], with a sector angle given by

$$\varphi_s = \arccos\left(\frac{2l_1^2 - l_2^2}{2l_1^2}\right). \tag{5}$$

Comprehensive mathematical modeling and parameterization of the eggbox structure is provided in [54] and [55].

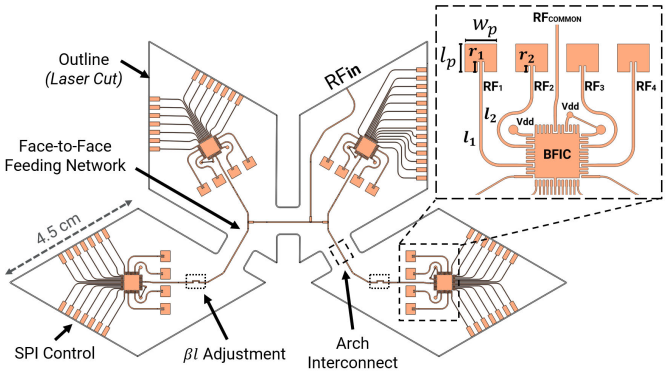

Fig. 4. Two-dimensional mapped layout of the proposed eggbox antenna array.

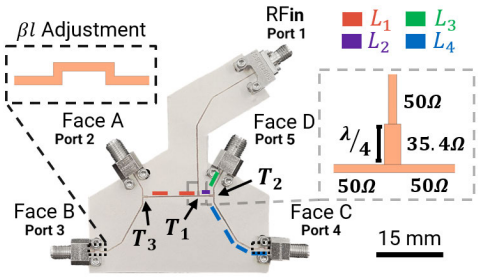

Fig. 5. Fabricated geometrically constrained and nonsymmetric four-port T-junction-based feeding network.

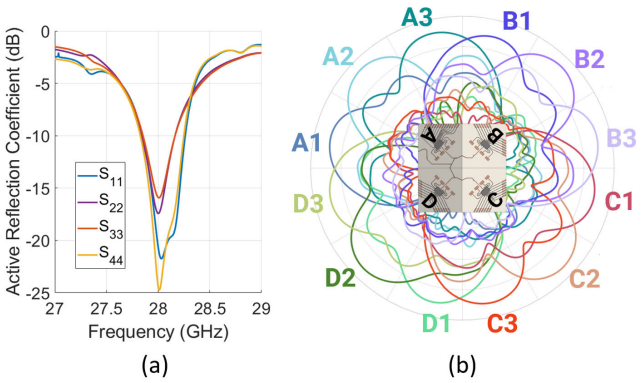

Fig. 6. (a) Simulated active reflection coefficient of the four patch antenna elements on a single face. (b) Simulated electronic beamsteering using BFICs A–D on each eggbox face and using three BFIC configurations.

B. Eggbox Phased Array Design

The 2-D planar layout of the proposed unit cell is shown in Fig. 4 and consists of four individually controlled faces. Each face consists of a linear four-element patch antenna array, controlled by an AWMF-0108 beamformer RFIC through a serial peripheral interface (SPI). The AWMF-0108 is a 28-GHz quad-core IC supporting four radiating elements and TX/RX half-duplex operation, with integrated amplifiers and phase shifters. The amplifiers are capable of providing amplitude increments of 1 dB, and the phase shifters are capable of providing phase increments of 11.25°. The patch antenna elements are designed at 28 GHz in CST Microwave Studio on the 3-D eggbox structure in its natural unfolded state, as shown in Fig. 1(b). The elements are inset-fed and placed half a wavelength apart to provide the largest steerable beam angle range while avoiding grating lobes. They have dimensions of $l_p = 2.95$ mm, $w_p = 3.37$ mm, $r_1 = 1.07$ mm, and $r_2 = 0.65$ mm, which takes mutual coupling effects into account.

The four beamformer ICs on each of the four eggbox faces have a common RF input/output, facilitated through a face-to-face feeding network. Due to the dynamic 3-D morphology of the eggbox structure, a symmetric feeding network is not feasible. As such, ensuring phase/amplitude power balance across all four branches becomes a nontrivial task. While any phase/amplitude imbalance can be compensated for using the beamformer ICs, it is imperative to highlight the 11.25° discrete phase resolution of the utilized beamformer IC. As shown in Fig. 4, tuning the lengths of the four branches is constrained by the fixed location of the input and four output ports determined by the position of the beamformer ICs. Adjusting the length of the branch transmission lines is, therefore, achieved through a "U-Shaped" structure incorporated within two branches. As shown in Fig. 5, a four-port T-junction-based feeding network is designed and fabricated. Given that branches cannot be of equal length (e.g., L_1 and L_2 or L_3 and L_4), optimization is carried out such that at every T-junction, the length difference of the two splitting branches is a multiple of $\lambda/2$ for no phase difference. Nevertheless, measurements of the fabricated prototype reveal a maximum amplitude and phase imbalance of 0.8 dB and 15°, respectively. This is accounted for using the beamformer IC, resulting in a maximum amplitude and phase imbalance of 0.2 dB and 3.75°, respectively, and is found to have negligible effect on the beamsteering performance of the eggbox phased array.

The simulated active reflection coefficients as seen by a beamformer IC are shown in Fig. 6(a) for the four elements excited with the required phases to radiate simultaneously, radiating a beam at boresight. This phase takes into account the needed phase compensation due to not only the face-to-face feeding network but also the different transmission line lengths connecting the patch elements to the BFIC's RF ports. Moreover, the total efficiency of the elements is found to be −2.36 dB at the frequency of resonance.

Looking at the eggbox phased array as a multisurface array, one possible operating mechanism is to use one face (surface) at a time. The beam from one planar face is phase-steered to the maximum edge of the steering range at which the adjacent plane face takes over. Fig. 6(b) shows the simulated radiation pattern of nine individual beams overlaid in the azimuth plane. Each eggbox face (*A*–*D*) covers one quadrant of the azimuth plane, ensuring a continuous 360° angular coverage. The radiation patterns of single-face activation operation are also plotted in the 2-D plane in Fig. 7. For a uniformly spaced linear array separated with interelement spacing d, the required phase difference applied to each element i to steer the beam by an angle θ from boresight is given by

$$\Delta\phi_i = \frac{2\pi}{\lambda} d \sin(\theta). \tag{6}$$

Activating all four beamformer ICs of an eggbox unit-cell results in the radiation patterns shown in Fig. 8. Applying the required element phases to each of the four patch elements on each eggbox face to beam at boresight produces four independent diagonal beams [see Fig. 8(a)]. Steering the beams

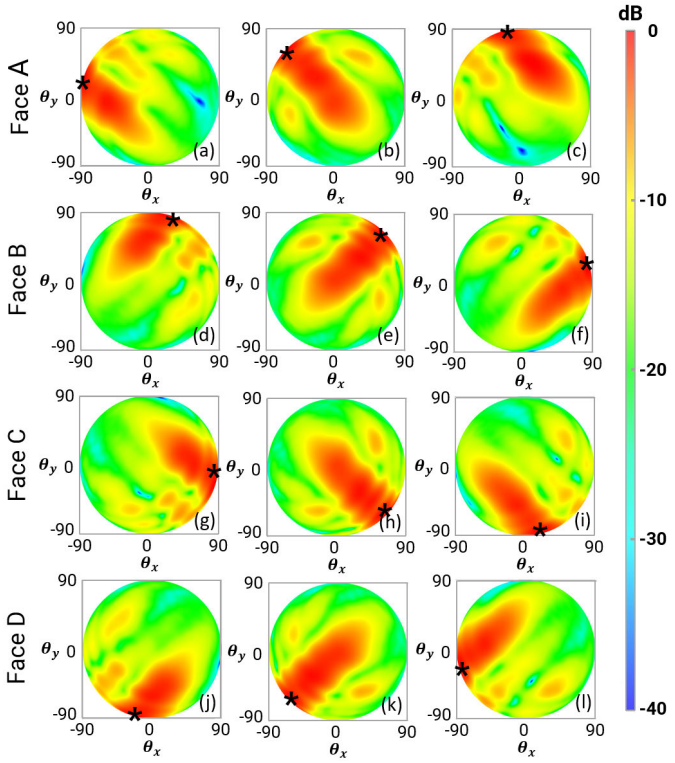

Fig. 7. Simulated 2-D patterns of a 16-element unit-cell eggbox. Selective activation and three beamsteering configurations for (a)–(c) face A, (d)–(f) face B, (g)–(i) face C, and (j)–(l) face D. * indicates maximum gain.

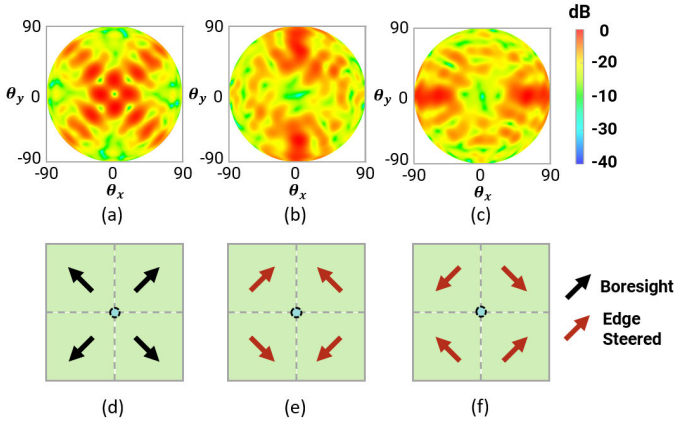

Fig. 8. Simulated 2-D patterns of a 16-element unit-cell unfolded ($\alpha = 90°$) eggbox phased array. All faces are activated, and beamforming is utilized to modify the radiation patterns from (a) four-beam to (b) and (c) two-beam configurations, with the corresponding beamforming maps shown in (d), (e), and (f), respectively. Each quadrant represents an eggbox face (four elements) with the arrows indicating the beamsteering configuration applied.

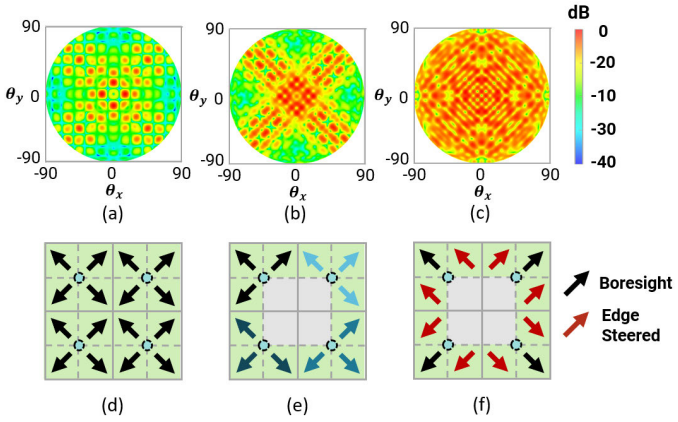

Fig. 9. Simulated 2-D patterns of a 64-element unfolded ($\alpha = 90°$) eggbox phased array (2 × 2 unit cell). Activated faces are shown in green, and beamforming is utilized to modify the radiation patterns from (a) and (b) four beams to (c) quasi-isotropic radiation patterns. The corresponding beamforming maps are shown in (d)–(f), were each quadrant represents an eggbox unit cell (16 elements) with the arrows indicating the beamsteering configuration applied to a face.

to $\theta \approx 40°$ in the directions illustrated in the beamsteering maps shown in Fig. 8(e) and (f) results in a constructive combination, producing two beams along the x- or y-axis.

Building on that, a 2 × 2 unit-cell eggbox phased array (64 elements) is simulated in its natural unfolded state. The radiation patterns for a select number of beamforming configurations are shown in Fig. 9(a)–(c) with the corresponding beamforming maps shown in Fig. 9(d)–(f). In Fig. 9(a), all 16 faces are electronically configured to beam at boresight. In Fig. 9(b), the 12 outer faces are activated to beam at boresight, with the four inner faces turned off. Moreover, while all faces are still beaming at boresight, an additional phase shift of $\Delta\phi = 90°$ is sequentially applied to each eggbox unit cell. That is, the activated elements of the top-right eggbox are beaming at boresight and are 90° out-of-phase with respect to the top-left unit-cell eggbox. Similarly, the bottom-right and bottom-left unit cells are 180° and 270° out-of-phase with respect to the top-left unit cell, respectively. While the resulting radiation pattern is still of a diagonal four-beam configuration, the position of the nulls and peaks have been manipulated. Due to the unique 3-D morphology of the eggbox origami structure and consequently the spatial position and orientation of antenna elements, the phase difference $\Delta\phi$ applied to the elements may be with respect to other elements on the same face, different faces of an eggbox unit cell, or with respect to other unit cells. This framework presents a plethora of possible configurations, of which we have only presented a select few for demonstration purposes. Finally, a quasi-isotropic radiation pattern is obtained in Fig. 9(c) by applying the beamforming scheme in Fig. 9(f).

The concept of manipulating the position of the radiation pattern's nulls and peaks is further explored with a unit cell and 2 × 2 unit-cell eggbox phased array, as shown in Fig. 10. In both cases, half the number of faces is activated to produce two diagonal beams for demonstration purposes. While all antenna elements are beaming at boresight, a 180° phase difference is applied to the elements of opposite faces in Fig. 10(d)–(f) and (j)–(l). This is illustrated using arrows of two colors on the beamforming maps in Fig. 10(f) and (l). Complementary patterns are shown between the two beamforming configurations of each phased array were the position of the nulls and peaks are interchanged. On the 1-D patterns of a plane cut along the direction of the beam [see Fig. 10(b), (e), (h), and (k)], the positions of the nulls at 0°, ±15°, ±30°, and so on are interchanged with peaks when a phase shift of $\Delta\phi = 180°$ is applied as aforementioned.

Finally, a 64-element (2 × 2 unit cell) eggbox phased array is mechanically folded along the y-axis to a fold angle of

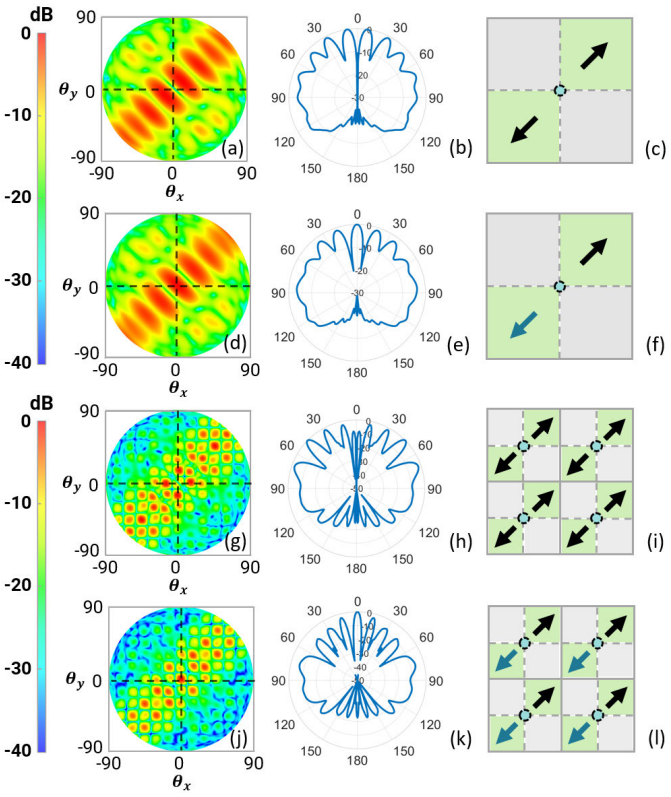

Fig. 10. Simulated 2-D patterns, 1-D cuts, and corresponding beamforming maps of unfolded ($\alpha = 90°$) eggbox array structures with half the number of faces activated, producing two beams. Complimentary patterns are demonstrated where nulls are transformed to peaks and vice versa through beamforming for (a)–(f) a unit cell (16-element) and (g)–(l) 2 × 2 unit-cell (64-element) eggbox. The arrows indicate the beamsteering configuration applied to a face. While all activated faces are configured to beam at boresight, the blue arrows have a phase offset of 180° relative to the black arrows.

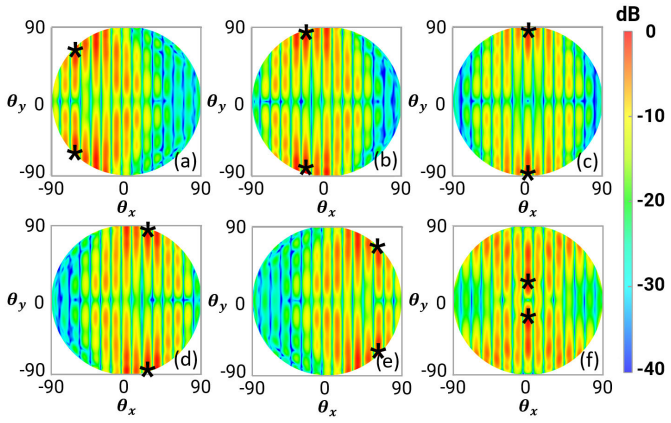

Fig. 11. Simulated 2-D patterns of a folded ($\alpha = 18°$) 2 × 2 unit-cell (64-element) eggbox phased array. Beamforming is utilized to steer the beam(s) to the (a), (b) left, (c) exterior-center, (d), (e) right, and (f) interior-center.

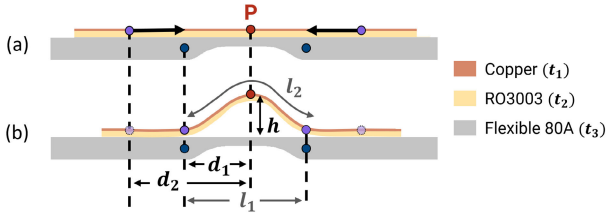

Fig. 12. Construction of the proposed "arch" interconnect. (a) Rogers substrate is initially laid flat on the flexible mechanical structure and then (b) adjusted according to the values of d_1 and d_2. The stackup thicknesses are $t_1 = 0.035$ mm, $t_2 = 0.13$ mm, and $t_3 = 1.27$ mm.

$\alpha = 18°$ (compressed state). The outer faces are then activated, and the beamforming is utilized to steer the beams to various positions in the 2-D plane. This is simulated in Fig. 11 for two beams—steering from the far left [see Fig. 11(a)] to the far right [see Fig. 11(e)] and from the outer edges [see Fig. 11(c)] to the center [see Fig. 11(f)].

IV. Fabrication

This section outlines the eggbox phased array fabrication process. Section IV-A covers the design of an additively manufactured foldable interconnect, enabling the fully contained, shape-changing phased array discussed in Section IV-B. Section IV-C presents an umbrella-inspired mechanical actuator to control the folding angle.

A. Fully Foldable mm-Wave Hinge Interconnect

As aforementioned, the designed face-to-face feeding network extends over foldable hinges required to realize the eggbox origami. While efforts have been directed at designing flexible [56] and stretchable [57] additively manufactured interconnects, it is imperative to note that these efforts differ from the challenge of fully bending interconnects over a small radius ($r \leq 2$ mm) due to the high levels of applied tensile and compressive stresses.

The absence of a robust solution to this specific bending requirement has, up until now, hindered the realization of fully contained origami antenna arrays at this miniaturized scale and at mm-wave frequencies. Our proposed foldable "arch" hinge interconnect, as shown in Fig. 12, successfully addresses this challenge. It is the first additively manufactured flexible interconnect that not only withstands static bends (unchanging deformation) but is also durable enough to endure dynamic bends, repeatedly folding from its unfolded state (0°) to its fully folded state (180°).

The stackup consists of a flexible 3-D printed hinge for mechanical support and a flexible Rogers RO3003 substrate (130 μm thick) onto which a 50-Ω transmission line is inkjet-printed using the fabrication process detailed in Section IV-B. The RO3003 substrate is initially laid flat on the flexible mechanical structure [see Fig. 12(a)], and then, two points on the substrate located at a distance d_2 from the center of the hinge are shifted to the fixed points on the mechanical structure located at a distance d_1 [see Fig. 12(b)]. This effectively forms the "arch" interconnect topology. In this configuration, the flexible substrate is arched upward in the unfolded state, reducing the stresses exerted on the interconnect when folded. Essentially, the interconnect's midpoint, denoted as "P," experiences no stress. This allows for repeated folds without observing any microcracks or a change in resistance and RF performance of the printed conductor trace.

A fabricated "arch" interconnect is shown in Fig. 13(a), where $d_1 = 8$ mm and $d_2 = 10.5$ mm have been used. Consequently, the arch height (h) is found to be 13.78 mm,

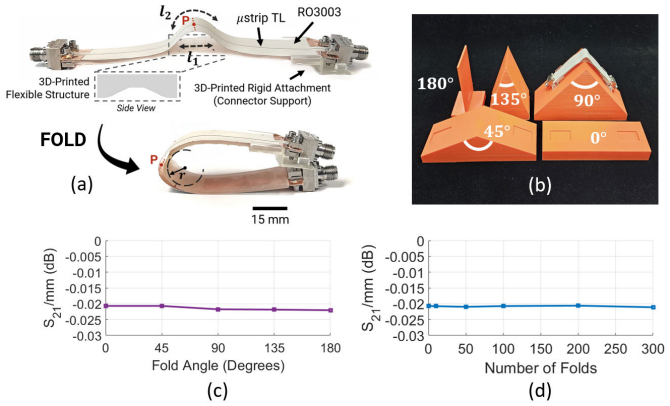

Fig. 13. (a) Fabricated "arch" interconnect. (b) Three-dimensional printed fixtures for various bend angles. Measured transmission coefficient for different (c) fold angles and (d) bend cycles at 28 GHz. Note that $l_2 \geq l_1$.

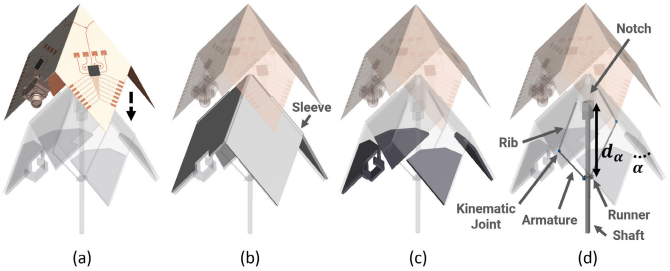

Fig. 14. Mechanical stackup (a) inkjet-printed phased array, face-to-face feeding network, and beamformer ICs on a Rogers RO3003 substrate, (b) flexible mechanical structure with integrated sleeves, (c) rigid support structures, and (d) umbrella-inspired actuation mechanism.

which can be approximated by

$$h \approx \frac{(d_1 + \Delta d)^2}{d_1} = \frac{d_2^2}{d_1} \tag{7}$$

where $\Delta d = d_2 - d_1$. Furthermore, it is to be noted that the length l_2 of the arch interconnect is $2\Delta d$ longer than the flat interconnect of length l_1, where

$$l_1 = 2d_1 \tag{8}$$

$$l_2 \approx 2(d_1 + \Delta d) = 2d_2. \tag{9}$$

Interconnect test fixtures of different bend angles are 3-D printed and shown in Fig. 13(b). RF measurements validate near identical performance for different bend angles [see Fig. 13(c)] and no degradation in performance until at least 300 folds [see Fig. 13(d)] with S_{21} remaining near constant at -0.02 dB/mm for all folding angles between 0° and 180° and throughout the frequency range of 24–32 GHz. These results provide strong evidence that the measurements presented in Section V are both repeatable and reproducible.

B. Additively Manufactured Eggbox Phased Array

The fabrication process of the proposed origami-inspired phased array involves a streamlined four-stage approach, as illustrated in 14. The phased array elements, feeding network, and bias lines are first inkjet-printed on a flexible substrate, with the beamformer ICs subsequently attached [see Fig. 14(a)]. This substrate is then adhered onto a flexible 3-D printed eggbox origami structure [see Fig. 14(b)] with the addition of rigid 3-D printed support structures for improved mechanical durability [see Fig. 14(c)]. Finally, the eggbox phased array is affixed onto the actuation mechanism [see Fig. 14(d)], as discussed in Section IV-C.

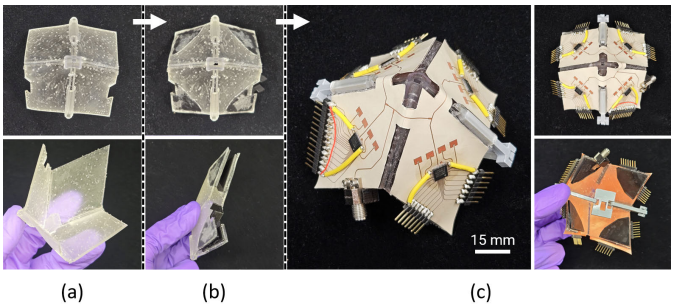

Fig. 15. Fabrication process: (a) flexible 3-D printed eggbox origami structure, (b) 3-D printed rigid support structures added for mechanical robustness, and (c) fully assembled eggbox phased array unit cell.

First, the phased array is additively manufactured using an inkjet-printed masking technique followed by chemical etching. The patch elements and RF circuitry are inkjet-printed onto a flexible Rogers RO3003 substrate, with $\varepsilon_r = 3.0$, $\tan\delta = 0.001$, and a thickness of $h = 130$ μm. The inkjet printing involves depositing six layers of SU-8 photoresist utilizing the Fujifilm Dimatix DMP-2831 inkjet printer and using a Samba cartridge with a drop volume of 2.4 pL. Following this, a UV crosslinker cures the resulting pattern, which is then submerged in a ferric chloride ($FeCl_3$) bath, etching any exposed copper. Finally, the substrate is washed with acetone (dimethyl ketone) to remove the SU-8 dielectric layers. To ensure efficient thermal management, a 3×3 via array, featuring 0.2 mm via hole diameters, is mechanically drilled into the BFIC's ground pad and subsequently filled with conductive silver paste (LPKF ProConduct; $\rho = 9.42 \times 10^{-6}$ Ωm). The substrate then undergoes thermal sintering at 160 °C for 30 min. Solder paste (63Sn/37Pb) is then applied to all pads, followed by solder reflow utilizing a heat gun to affix the four 6×6-mm QFN packaged beamformer ICs. Finally, header pins are soldered to provide access to the biasing and SPI control lines.

Second, an origami eggbox unit cell is designed in a 3-D CAD software, implementing mathematical formulations, as outlined in Section III-A, and incorporating the proposed hinge structure discussed in Section IV-A. The origami structure is 3-D printed using a Formlabs Form 3+ stereolithography (SLA) printer, utilizing Formlabs flexible80A, a flexible photopolymer resin, as shown in Fig. 15(a). Flexible80A is a translucent elastomer with a rubber-like feel that is able to withstand bending, even through repeated cycles, while still having the structural strength to keep its shape. While it is only necessary for the four hinge sections to be flexible (foldable), utilizing a single-body/single-material mechanical structure where the hinges are integrated with the mechanical structure facilitates the fabrication process. The SLA 3-D printed Flexible80A structure is both mechanically durable and flexible enough to allow the integration of foldable hinge sections. Moreover, the orientation during 3-D printing and

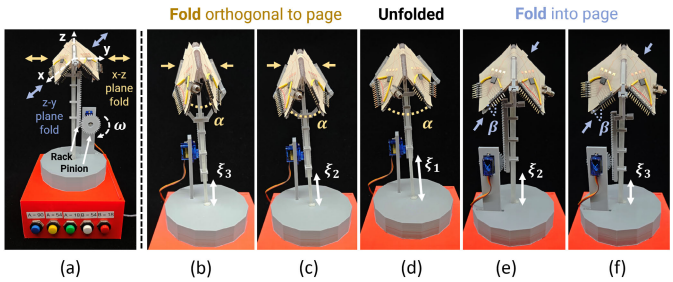

Fig. 16. (a) Umbrella-inspired actuation mechanism, folding along α in the xz plane and along β in the zy plane. Eggbox phased array in different folding configurations. (b) $\alpha = 18°$, (c) $\alpha = 54°$, (d) $\alpha = \beta = 90°$, (e) $\beta = 54°$, and (f) $\beta = 18°$. ξ denotes the distance from the base to the lower edge of the linear gear.

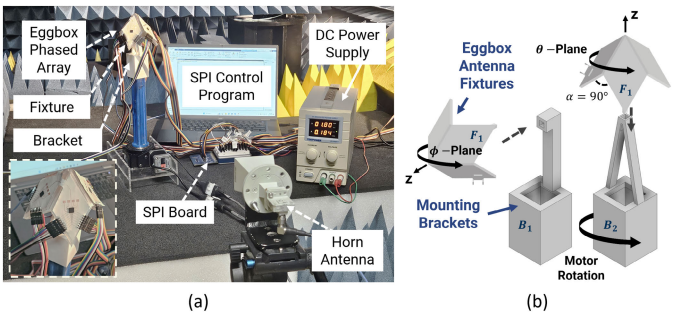

Fig. 17. (a) Radiation pattern measurement setup. (b) Mounting brackets (for different plane cuts) and antenna fixtures (for different bend angles).

the UV curing duration were found to be crucial parameters, impacting hinge flexibility. A different curing duration affects the rigidity of the material due to the change in the material's particle alignment. To solidify the material, the printed structure undergoes sonication in an IPA bath for 20 min, followed by a 15-min UV curing treatment, which was found to be optimal.

Third, to improve mechanical robustness and facilitate operability, 3-D printed rigid support structures are affixed onto the eggbox structure. These structures, as shown in Fig. 15(b), increase the rigidity of the four eggbox faces, which was found to be particularly beneficial in supporting the additional weight of the RF connector, RF coaxial cable, and beamformer IC bias jumper wires used for measurement purposes in Section V-B. The structures, printed using a fused deposition modeling (FDM) 3-D printer utilizing a PLA filament, are precisely designed to avoid obstructing the folding action of the eggbox origami.

Finally, the substrate with integrated beamformer ICs is affixed onto the flexible 3-D printed origami structure using an adhesive, as shown in Fig. 15(c). A 2.92-mm narrow block Southwest End Launch connector is then attached, followed by an assembly to the actuation mechanism, as discussed in Section IV-C. The resulting eggbox phased array, weighing 44 g and occupying a maximum volume of 6.36 cm^3 in its natural unfolded state, exemplifies the success of this fully contained, lightweight, and compact prototype achieved through additive manufacturing.

C. Folding Actuation Mechanism

To fold the origami-inspired phased array to different folding angles, an umbrella-inspired actuation mechanism is designed, 3-D printed, and assembled. The mechanism consists of several key mechanical components, including a rib with kinematic joints that facilitate the movement of the armatures, a runner that slides along the shaft, and a shaft that provides structural support and a pathway for the runner's movement [see Fig. 14(d)]. A notch in the flexible eggbox structure allows it to secure onto the shaft, and hollow sleeves allow the attachment to the actuation mechanism's ribs.

As shown in the fabricated prototype of Fig. 16(a), a circular gear (pinion) is attached to a servo motor (SG90 microservo), which drives a linear gear (rack). The linear gear, in turn, translates the rotational motion of the circular gear into linear motion through

$$d_\alpha = d_{90} + r\Delta\omega \tag{10}$$

where d_α is the distance from the fixed notch to the runner when the eggbox is at a folding angle α (degrees), r is the radius of the circular gear, and ω is the angular rotation in radians.

The linear motion of the linear gear then moves the runner along the shaft, which leads to a change in the folding angle of the eggbox phased array. The folding angle, α, is mapped to the linear distance through the nonlinear relation given by

$$\alpha = 2 \times \arccos\left(\frac{d_\alpha^2 - L_{\text{arm}}^2 + L_{\text{rib}}^2}{2L_{\text{rib}} \cdot d_\alpha}\right) \tag{11}$$

where L_{arm} and L_{rib} are the designed lengths of the armature and rib, respectively, as illustrated in Fig. 14(d). Practically, and due to symmetry, $18° \leq \alpha \leq 90°$. Consequently, this leads to $0 \leq \Delta\omega \leq {}^1/_r(d_{18} - d_{90}) = 2.57$ rad $= 0.4$ revolutions. For $\Delta\omega = 0$, $d_\alpha = d_{90} = 48.3$ mm, and rotating the servo motor by $\Delta\omega$ increases d_α, which consequently decreases α.

An Arduino Nano microcontroller is used to drive the servo motor, and a control program is written to adjust the eggbox folding angle according to (10) and (11). Push buttons with preset folding angles are also used for demonstration purposes, as shown in Fig. 16(a). The eggbox phased array is attached to the actuation mechanism and folded to various angles, as shown in Fig. 16(b)–(f). The proposed actuation mechanism can change the shape of the eggbox phased array from its natural unfolded state ($\alpha = \beta = 90°$) to its folded state ($\alpha = 18°$) in less than 255 ms and provides an angular precision of $\Delta\alpha = \pm 0.4°$ at worst.

V. Measurements

The 2-DOF mechanical and electrical reconfigurability of the eggbox phased array is demonstrated. Section V-A measures radiation patterns for various electrical/mechanical configurations, while Section V-B validates the prototype's performance in a real-world communication testbed.

A. Reconfigurable Radiation Pattern Measurements

The radiation patterns of the fabricated prototype are measured in an anechoic chamber [see Fig. 17(a)] for different eggbox bend angles (mechanical reconfigurability) and beamformer IC configurations (electrical reconfigurability). Rigid

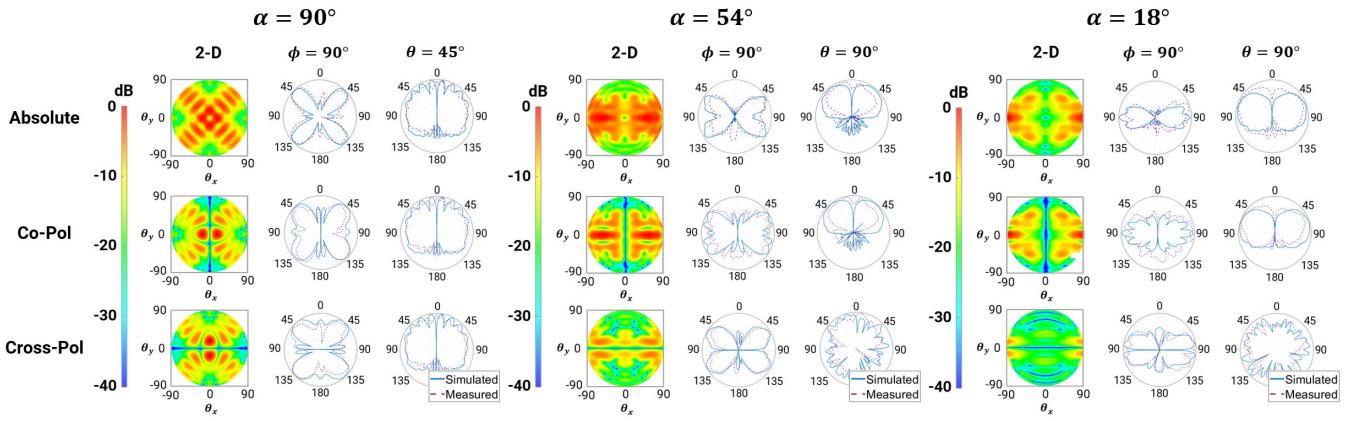

Fig. 18. Simulated and measured normalized radiation patterns for eggbox mechanical bend angles of $\alpha = 90°$, $\alpha = 54°$, and $\alpha = 18°$.

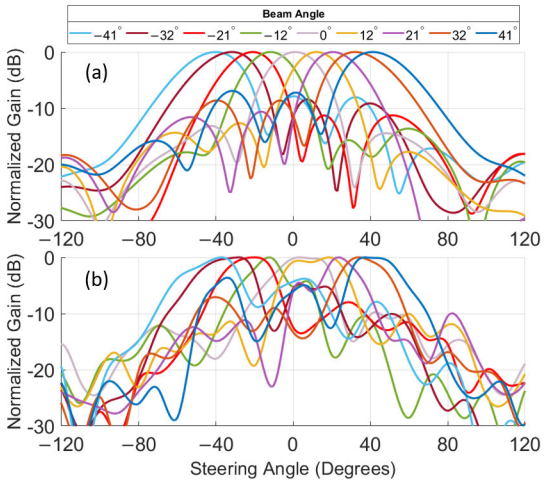

Fig. 19. (a) Simulated and (b) measured electronic beamsteering capability of a selectively activated eggbox face.

3-D printed fixtures for three different eggbox bend angles ($\alpha = 18°$, 54°, and 90°) are designed and used to attach the eggbox phased array onto an automatic antenna rotator system. This attachment is done through other 3-D printed mounting brackets that allow rotation in the azimuth or elevation planes or in the plane normal to an eggbox face, as shown in Fig. 17(b).

The beamformer ICs (AWMF-0108) are powered using a 1.8-V power supply and controlled through an SPI protocol. All SPI control lines from the beamformer ICs are connected to the NI USB-8452 master interface, which, in turn, provides a single USB connection to a computer. The beamformer ICs are connected in a daisy-chain topology that allows for multiple BFICs to be configured serially through a MATLAB script.

1) Radiation Pattern Reconfigurability Due to Mechanical Shape Change: Initially, the beamformer ICs are configured such that each planar face would beam at boresight. Measurements are taken in two plane cuts (θ and ϕ cuts), as defined by the coordinate system illustrated in Figs. 17(b) and 20. In each plane, the cross-polarization and copolarization patterns are measured and plotted against simulated patterns. The resulting normalized absolute patterns are also compared to the simulated patterns, as shown in Fig. 18, for three different mechanical fold angles: $\alpha = 90°$ (uncompressed), $\alpha = 54°$, and $\alpha = 18°$ (fully compressed). The measured and simulated results demonstrate a high degree of agreement. Any slight discrepancies fall within the expected tolerances for such systems and are justified by the manual additive manufacturing fabrication process of the prototype. In addition, since the flexible substrate onto which the antenna elements are printed is manually positioned onto the flexible eggbox structure, slight errors in the distance between antenna elements of different eggbox faces exist (refer to Fig. 15). Folding the eggbox phased array along the y-axis (decreasing α) enables a seamless transition in the radiation pattern, transforming it from four independent beams to a quasi-isotropic pattern and, finally, to two beams along the y-axis. By folding along the x-axis instead, symmetrical patterns can be achieved. For a given bend angle, the position of the pattern's nulls, beamwidth, and gain can then be independently controlled by providing the right phase conditions to the 16 radiating elements using the beamformer ICs.

Furthermore, it is worth remarking that when the eggbox phased array is in the natural uncompressed state ($\alpha = 90°$), the structure is completely symmetric, and as such, the cross-polarization and copolarization radiation patterns are identical in the ϕ plane and rotated by 90° (clockwise) in the θ plane. In the uncompressed state, the eggbox phased array is, therefore, circularly polarized. As the eggbox phased array folds and the spatial position and orientation of the elements change, the phased array's polarization is transformed toward a more linear polarization or, more specifically, an elliptical polarization with a high axial ratio. The result is clearly shown through the radiation patterns of the eggbox phased array in the compressed state ($\alpha = 18°$). In that mechanical state, eight antenna elements (four elements on two adjacent faces) form a "∨" shaped array. The maximum realized gain of the cross-polarization measurement in the ϕ plane is −34.8 dBi, clearly demonstrating that the phased array is almost linearly polarized. Moreover, the absolute radiation pattern is nearly identical to the copolarization pattern.

2) Radiation Pattern Reconfigurability due to Electrical Beamsteering: Next, a planar face (four radiating elements) is selectively activated to demonstrate the beamsteering capability. The steering range is simulated [see Fig. 19(a)] and measured [see Fig. 19(b)] at 28 GHz, and good agreement

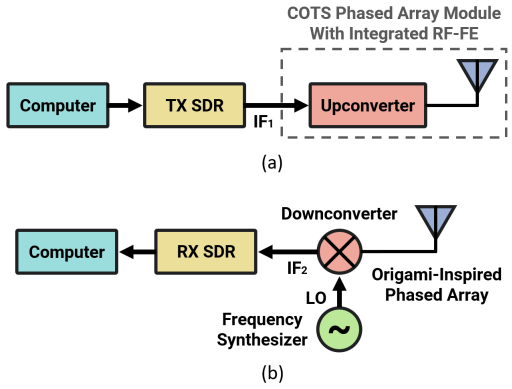

Fig. 20. Block diagram of (a) transmit and (b) receive RF chains.

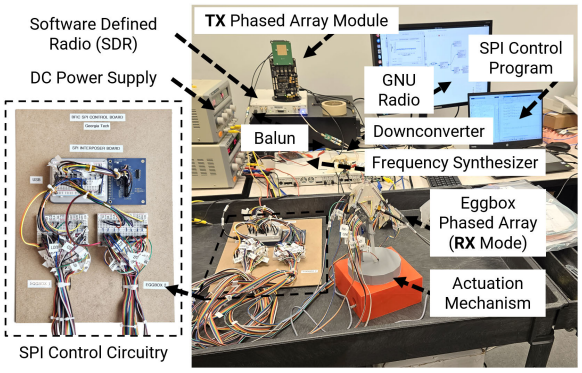

Fig. 21. SDR testbed measurement setup.

is shown. The −3-dB steering range (at which the gain drops by 3 dB relative to the main beam power) was found to reach ±54°. A SLL of −7.0 (simulated) or −4.2 dB (measured), however, results in a steering angle range of ±41°. An increase in the measured SLL can be explained as a result of fabrication tolerances and the presence of a large number of cables for digital control. In general, increasing the number of radiating elements from four per eggbox face would decrease the SLL, in addition to decreasing the beamwidth, and, as a result, increasing directivity. Amplitude tapering can also be applied to improve the performance. A slight asymmetry in the measured results can be explained by measurement errors, such as a slight misalignment between the horn antenna and eggbox phased array, which is manually carried out. Moreover, any slight misalignment is more pronounced in the eggbox phased array due to the 3-D arrangement of the individual elements (compared to a planar antenna).

The measured gain of a single four-element eggbox face is 5.6 dB at boresight (main beam power) and reaches 9.6 dB if the beamformer IC is utilized for amplification. The dc power consumed by a single face is around 882 mW if the beamformer is to be used in the transmit mode, 576 mW if to be used in the receive mode, and 48.8 mW in the standby mode.

B. System-Level Communication Testbed Demonstration

To further demonstrate the functionality and robustness of the additively manufactured origami-inspired phased array, a real-world communication testbed is set up to transmit a 54-MB video file. A 28-GHz OFDM-based testbed is put up,

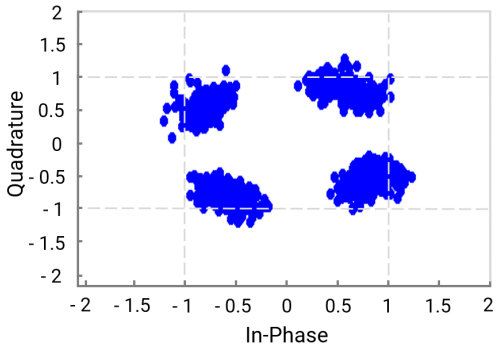

Fig. 22. Measured constellation diagram of the demodulated QPSK signal received by the origami-inspired phased array.

utilizing commercial-off-the-shelf components for the transmit and receive RF chains, with the origami-inspired phased array used as the receiver chain's antenna.

The transmit chain, as shown in Fig. 20(a), consists of a Linux-based computer machine, a software-defined radio (SDR), and a phased array module with an integrated RF front end. The SDR (USRP X310), capable of covering dc-6-GHz with up to 160 MHz of baseband bandwidth, is controlled by the GNU Radio development framework and is programmed to perform QPSK modulation with an output intermediate frequency (IF) of 3.5 GHz. The Sivers EVK02004 module then upconverts the signal to 28 GHz and transmits it through its integrated 4 × 4 element phased array. At the receiver chain [see Fig. 19(b)], the origami-inspired phased array is used in RX mode to receive the incoming 28-GHz signal. The ADMV1014 downconverter is then used in conjunction with the ADF5355 frequency synthesizer to output a 4.8-GHz downconverted signal. Finally, the signal is processed by the USRP X310 SDR. The measurement setup is shown in Fig. 21.

The quality of the measured demodulated signal is visualized through the IQ constellation plot, as shown in Fig. 22. As illustrated, the QPSK constellation, consisting of four equally spaced signal points, is clearly reconstructed. Further signal processing techniques can be employed to enhance signal clarity. As aforementioned, since an OFDM-based system is utilized, the issue of carrier frequency offset (CFO) naturally arises. CFO, which describes the mismatch between the carrier frequencies at the transmitter and receiver, is one of many nonideal conditions that may affect signal integrity. While a CFO of 0.1 MHz is measured (4.7999 GHz compared to 4.8 GHz), the received signal is still successfully decoded. In addition, an error vector magnitude (EVM) of −15.4 dB is measured, which is adequate for demonstration purposes considering the multitude of RF modules used in the transmit and receive chains, the additively manufactured prototype, and the limited signal processing algorithms utilized. The video file is successfully transmitted and received using the origami-inspired phased array with an average measured throughput of 1.2 Gb/s. Therefore, it takes approximately 0.36 s to receive the entire 54-MB file.

VI. Conclusion

This article presents the design, fabrication, actuation, and calibration of an origami-inspired eggbox phased array at

mm-wave frequencies. As the first shape-changing phased array realized at a millimeter scale, it demonstrates unparalleled capabilities in radiation pattern reconfigurability, utilizing two-degree-of-freedom (2-DOF) mechanical shape change and electrical beamsteering. By breaking the tradeoff between gain and angular coverage, the eggbox phased array addresses the limitations of conventional planar arrays and prior origami-inspired designs. The additively manufactured eggbox phased array is multifaceted, enabling multibeam capabilities, fully contained with on-structure beamforming ICs and a flexible feeding network for high integration levels, and is modular and tile-based, allowing for a scalable design. The eggbox phased array is utilized in an OFDM-based mm-wave communication testbed to decode a QPSK-modulated video file at a throughput of 1.2 Gb/s, demonstrating the validity of the additively manufactured prototype in a real-world scenario.

This article also lays the foundational framework for a new category of shape-changing phased arrays, emphasizing the multidisciplinary efforts required, including multimaterial fabrication techniques, programmable folding mechanisms, and beam-shaping/calibration methods. While this initial demonstration showcased a select set of presynthesized codebook-based radiation patterns, future breakthroughs in real-time ML/AI-enabled 4-D pattern synthesis algorithms will enable arbitrary beam shaping of morphing phased arrays, unlocking unprecedented potential for massive MIMO systems. Concurrently, the development of custom measurement setups with batch measurement capabilities and advanced testing protocols will allow for a comprehensive characterization of the near-limitless combinations of geometric tessellations and electronic beamforming configurations. Moreover, advancements in flexible, additively manufactured multilayer stackups will improve the digital routing of beamformer ICs between eggbox faces, reducing the number of external control wires and resulting in more compact and integrated structures. Finally, the development of programmable materials and novel actuation mechanisms for origami structures will enable the scalability to large-scale $(n \times n)$ unit cells, enhancing beamsteering precision, gain, coverage angles, and radiation pattern reconfigurations. These advancements will drive a paradigm shift in 5G/beyond-5G sensing and communication applications for digital awareness.

ACKNOWLEDGMENT

The views and conclusions contained in this document are those of the authors and should not be interpreted as representing the official policies, either expressed or implied, of the Naval Information Warfare Center or U.S. Government. The U.S. Government is authorized to reproduce and distribute reprints for government purposes notwithstanding any copyright notation herein.

REFERENCES

[1] J. Costantine, Y. Tawk, S. E. Barbin, and C. G. Christodoulou, "Reconfigurable antennas: Design and applications," *Proc. IEEE*, vol. 103, no. 3, pp. 424–437, Mar. 2015.

[2] X. Liu, S. Yao, N. Russo, and S. Georgakopoulos, "Tri-band reconfigurable origami helical array," in *Proc. IEEE Int. Symp. Antennas Propag. USNC/URSI Nat. Radio Sci. Meeting*, Jul. 2018, pp. 1231–1232.

[3] S. I. H. Shah, S. Gosh, M. M. Tentzeris, and S. Lim, "A novel bio inspired pattern reconfigurable quasi-yagi helical antenna using origami DNA," in *Proc. Int. Symp. Antennas Propag. (ISAP)*, Oct. 2018, pp. 1–2.

[4] W. Su, R. Bahr, S. A. Nauroze, and M. M. Tentzeris, "Novel 3D-printed 'Chinese fan' bow-tie antennas for origami/shape-changing configurations," in *Proc. IEEE Int. Symp. Antennas Propag. USNC/URSI Nat. Radio Sci. Meeting*, Jul. 2017, pp. 1245–1246.

[5] X. Liu, S. Yao, B. S. Cook, M. M. Tentzeris, and S. V. Georgakopoulos, "An origami reconfigurable axial-mode bifilar helical antenna," *IEEE Trans. Antennas Propag.*, vol. 63, no. 12, pp. 5897–5903, Dec. 2015.

[6] L. Wang et al., "Active reconfigurable tristable square-twist origami," *Adv. Funct. Mater.*, vol. 30, no. 13, Mar. 2020, Art. no. 1909087.

[7] S. Yao, X. Liu, and S. V. Georgakopoulos, "Morphing origami conical spiral antenna based on the Nojima wrap," *IEEE Trans. Antennas Propag.*, vol. 65, no. 5, pp. 2222–2232, May 2017.

[8] H. Choe and S. Lim, "Foldable multifunctional planar antenna array," in *Proc. Asia–Pacific Microw. Conf.*, Dec. 2012, pp. 1097–1099.

[9] S. V. Georgakopoulos et al., "Origami antennas," *IEEE Open J. Antennas Propag.*, vol. 2, pp. 1020–1043, 2021.

[10] S. I. H. Shah, S. Bashir, M. Ashfaq, A. Altaf, and H. Rmili, "Lightweight and low-cost deployable origami antennas—A review," *IEEE Access*, vol. 9, pp. 86429–86448, 2021.

[11] S. I. H. Shah and S. Lim, "Review on recent origami inspired antennas from microwave to terahertz regime," *Mater. Des.*, vol. 198, Jan. 2021, Art. no. 109345.

[12] M. W. Nichols, A. Gonzalez, E. A. Alwan, and J. L. Volakis, "An accordion-folding series-fed patch array with finite thickness: A folding technique for CubeSat arrays," *IEEE Antennas Propag. Mag.*, vol. 65, no. 3, pp. 77–82, Jan. 2023.

[13] M. Hamza, C. L. Zekios, and S. V. Georgakopoulos, "A thick origami reconfigurable and packable patch array with enhanced beam steering," *IEEE Trans. Antennas Propag.*, vol. 68, no. 5, pp. 3653–3663, May 2020.

[14] S. R. Seiler et al., "Physical reconfiguration of an origami-inspired deployable microstrip patch antenna array," in *Proc. IEEE Int. Symp. Antennas Propag. USNC/URSI Nat. Radio Sci. Meeting*, Jul. 2017, pp. 2359–2360.

[15] D. E. Williams, C. Dorn, S. Pellegrino, and A. Hajimiri, "Origami-inspired shape-changing phased array," in *Proc. 50th Eur. Microw. Conf. (EuMC)*, Jan. 2021, pp. 344–347.

[16] H. Al Jamal, C. Hu, N. Wille, K. Zeng, and M. M. Tentzeris, "Beyond planar: An additively manufactured, origami-inspired, and shape-changing RFIC-based phased array for near-limitless radiation pattern reconfigurability in 5G/mm-Wave applications," *IEEE Microw. Wireless Technol. Lett.*, vol. 34, no. 6, pp. 841–844, Jun. 2024, doi: 10.1109/LMWT.2024.3396026.

[17] L. Josefsson and P. Persson, *Conformal Array Antenna Theory and Design*. Hoboken, NJ, USA: Wiley, 2006.

[18] A. C. Fikes, M. Gal-Katziri, O. S. Mizrahi, D. E. Williams, and A. Hajimiri, "Frontiers in flexible and shape-changing arrays," *IEEE J. Microw.*, vol. 3, no. 1, pp. 349–367, Jan. 2023.

[19] D. E. Williams, *Shape-Changing Phased Arrays*. Pasadena, CA, USA: California Institute of Technology, 2022.

[20] X. Liu, S. Yao, S. V. Georgakopoulos, B. S. Cook, and M. M. Tentzeris, "Reconfigurable helical antenna based on an origami structure for wireless communication system," in *IEEE MTT-S Int. Microw. Symp. Dig.*, Jun. 2014, pp. 1–4.

[21] S. Venkatesh, D. Sturm, X. Lu, R. J. Lang, and K. Sengupta, "Origami microwave imaging array: Metasurface tiles on a shape-morphing surface for reconfigurable computational imaging," *Adv. Sci.*, vol. 9, no. 28, Oct. 2022, Art. no. 2105016.

[22] K. Hu, T. W. Callis, and M. M. Tentzeris, "Additively manufactured flexible on-package phased antenna arrays with integrated microfluidic cooling channels for 5G/mmWave system-on-package designs," *IEEE Microw. Wireless Technol. Lett.*, vol. 33, no. 6, pp. 899–902, Jun. 2023.

[23] S. Yao, X. Liu, J. Gibson, and S. V. Georgakopoulos, "Deployable origami Yagi loop antenna," in *Proc. IEEE Int. Symp. Antennas Propag. USNC/URSI Nat. Radio Sci. Meeting*, Jul. 2015, pp. 2215–2216.

[24] R. V. Martinez, C. R. Fish, X. Chen, and G. M. Whitesides, "Elastomeric origami: Programmable paper-elastomer composites as pneumatic actuators," *Adv. Funct. Mater.*, vol. 22, no. 7, pp. 1376–1384, Apr. 2012.

[25] D. Li et al., "Origami-inspired soft twisting actuator," *Soft Robot.*, vol. 10, no. 2, pp. 395–409, Apr. 2023.

[26] J. M. McCracken, B. R. Donovan, and T. J. White, "Materials as machines," *Adv. Mater.*, vol. 32, no. 20, 2020, Art. no. 1906564.

[27] W. Su, S. A. Nauroze, B. Ryan, and M. M. Tentzeris, "Novel 3D printed liquid-metal-alloy microfluidics-based zigzag and helical antennas for origami reconfigurable antenna 'trees,"' in *IEEE MTT-S Int. Microw. Symp. Dig.*, Jun. 2017, pp. 1579–1582.

[28] S. I. H. Shah and S. Lim, "Thermally beam-direction- and beamwidth-switchable monopole antenna using origami reflectors with smart shape memory polymer hinges," *IEEE Antennas Wireless Propag. Lett.*, vol. 18, pp. 1696–1700, 2019.

[29] S. I. H. Shah, A. Sarkar, and S. Lim, "Electromechanically deployable high-gain pop-up antenna using shape memory alloy and kirigami technology," *IEEE Access*, vol. 8, pp. 225210–225218, 2020.

[30] S. Park, E. Park, M. Lee, and S. Lim, "Shape-morphing antenna array by 4D-printed multimaterial miura origami," *ACS Appl. Mater. Interface*, vol. 15, no. 42, pp. 49843–49853, Oct. 2023.

[31] S. Jape et al., "Self-foldable origami reflector antenna enabled by shape memory polymer actuation," *Smart Mater. Struct.*, vol. 29, no. 11, Nov. 2020, Art. no. 115011.

[32] Q. Ge, C. K. Dunn, H. J. Qi, and M. L. Dunn, "Active origami by 4D printing," *Smart Mater. Struct.*, vol. 23, no. 9, Sep. 2014, Art. no. 094007.

[33] Q. Zhang et al., "Origami and kirigami inspired self-folding for programming three-dimensional shape shifting of polymer sheets with light," *Extreme Mech. Lett.*, vol. 11, pp. 111–120, Feb. 2017.

[34] J. Xue, Y. Ge, Z. Liu, Z. Liu, J. Jiang, and G. Li, "Photoprogrammable moisture-responsive actuation of a shape memory polymer film," *ACS Appl. Mater. Interfaces*, vol. 14, no. 8, pp. 10836–10843, Mar. 2022.

[35] S. A. Nauroze and M. M. Tentzeris, "A thermally actuated fully inkjet-printed origami-inspired multilayer frequency selective surface with continuous-range tunability using polyester-based substrates," *IEEE Trans. Microw. Theory Techn.*, vol. 67, no. 12, pp. 4944–4954, Dec. 2019.

[36] S. A. Nauroze and M. M. Tentzeris, "Fully inkjet-printed multilayer tunable origami FSS structures with integrated thermal actuation mechanism," in *IEEE MTT-S Int. Microw. Symp. Dig.*, Jun. 2019, pp. 1363–1366.

[37] S. Wu, J. Eichenberger, J. Dai, Y. Chang, N. Ghalichechian, and R. R. Zhao, "Magnetically actuated reconfigurable metamaterials as conformal electromagnetic filters," *Adv. Intell. Syst.*, vol. 4, no. 9, Sep. 2022, Art. no. 2200106.

[38] Z. Qi, M. Zhou, Y. Li, Z. Xia, W. Huo, and X. Huang, "Reconfigurable flexible electronics driven by origami magnetic membranes," *Adv. Mater. Technol.*, vol. 6, no. 4, Apr. 2021, Art. no. 2001124.

[39] Y. Kim, H. Yuk, R. Zhao, S. A. Chester, and X. Zhao, "Printing ferromagnetic domains for untethered fast-transforming soft materials," *Nature*, vol. 558, no. 7709, pp. 274–279, Jun. 2018.

[40] J. Kimionis, M. Isakov, B. S. Koh, A. Georgiadis, and M. M. Tentzeris, "3D-printed origami packaging with inkjet-printed antennas for RF harvesting sensors," *IEEE Trans. Microw. Theory Techn.*, vol. 63, no. 12, pp. 4521–4532, Dec. 2015.

[41] X. He and M. M. Tentzeris, "In-package additively manufactured sensors for bend prediction and calibration of flexible phased arrays and flexible hybrid electronics," in *IEEE MTT-S Int. Microw. Symp. Dig.*, Jun. 2021, pp. 327–330.

[42] B. D. Braaten et al., "A self-adapting flexible (SELFLEX) antenna array for changing conformal surface applications," *IEEE Trans. Antennas Propag.*, vol. 61, no. 2, pp. 655–665, Feb. 2013.

[43] A. Fikes, O. S. Mizrahi, and A. Hajimiri, "A framework for array shape reconstruction through mutual coupling," *IEEE Trans. Microw. Theory Techn.*, vol. 69, no. 10, pp. 4422–4436, Oct. 2021.

[44] M. Joshi, K. Hu, C. A. Lynch, Y. Cui, G. Soto-Valle, and M. M. Tentzeris, "Computer vision enabled calibration of additively manufactured conformal phased arrays utilizing 3-D depth sensing camera," *IEEE Trans. Microw. Theory Techn.*, early access, May 9, 2024, doi: 10.1109/TMTT.2024.3396412.

[45] S. Prasad, "Generalized array pattern synthesis by the method of alternating orthogonal projections," *IEEE Trans. Antennas Propag.*, vol. AP-28, no. 3, pp. 328–332, May 1980.

[46] M. Dinnichert, "Full polarimetric pattern synthesis for an active conformal array," in *Proc. IEEE Int. Conf. Phased Array Syst. Technol.*, vol. 137, Jul. 2000, pp. 415–419.

[47] O. Schmid, "Pattern properties of singly and doubly curved arrays," presented at the 2nd Eur. Workshop Conformal Antennas, The Hague, The Netherlands, Apr. 24–25, 2001.

[48] I. Gupta and A. Ksienski, "Effect of mutual coupling on the performance of adaptive arrays," *IEEE Trans. Antennas Propag.*, vol. AP-31, no. 5, pp. 785–791, Sep. 1983.

[49] Q. Huang, H. Zhou, J. Bao, and X. Shi, "Accurate DOA estimations using microstrip adaptive arrays in the presence of mutual coupling effect," *Int. J. Antennas Propag.*, vol. 2013, Mar. 2013, Art. no. 919545.

[50] X. Zhang, G. Liao, Z. Yang, X. Zou, and Y. Chen, "Effective mutual coupling estimation and calibration for conformal arrays based on pattern perturbation," *IET Microw., Antennas Propag.*, vol. 14, no. 15, pp. 1998–2006, Dec. 2020.

[51] S. Shahidizandi and S. R. Seydnejad, "Blind beamforming for conformal arrays," *IEEE Antennas Wireless Propag. Lett.*, vol. 16, pp. 940–943, 2017.

[52] H. Nassar, A. Lebée, and L. Monasse, "Curvature, metric and parametrization of origami tessellations: Theory and application to the eggbox pattern," *Proc. Roy. Soc. A, Math., Phys. Eng. Sci.*, vol. 473, no. 2197, Jan. 2017, Art. no. 20160705.

[53] Y. Cui, R. Bahr, S. V. Rijs, and M. Tentzeris, "A novel 4-DOF wide-range tunable frequency selective surface using an origami 'eggbox' structure," *Int. J. Microw. Wireless Technol.*, vol. 13, no. 7, pp. 727–733, Sep. 2021.

[54] R. Xie, Y. Chen, and J. M. Gattas, "Parametrisation and application of cube and eggbox-type folded geometries," *Int. J. Space Struct.*, vol. 30, no. 2, pp. 99–110, Jun. 2015.

[55] M. Schenk et al., "Origami folding: A structural engineering approach," *Origami*, vol. 5, pp. 291–304, Jan. 2011.

[56] J. Vaithilingam et al., "3D-inkjet printing of flexible and stretchable electronics," in *Proc. 26th Solid Freeform Fabr. Symp.*, Austin, TX, USA, 2015, pp. 10–12.

[57] T. Liimatta, E. Halonen, H. Sillanpää, J. Niittynen, and M. Mäntysalo, "Inkjet printing in manufacturing of stretchable interconnects," in *Proc. IEEE 64th Electron. Compon. Technol. Conf. (ECTC)*, May 2014, pp. 151–156.

Hani Al Jamal (Graduate Student Member, IEEE) received the B.E. degree (Hons.) in electrical and computer engineering from American University of Beirut, Beirut, Lebanon, and a minor in applied mathematics in 2022. He is currently pursuing the Ph.D. degree in electrical and computer engineering at Georgia Institute of Technology, Atlanta, GA, USA.

He is currently a Research Assistant with ATHENA Research Group, Georgia Institute of Technology, where he is involved in utilizing additive manufacturing techniques to design highly integrated, conformal, and morphing RF front-end circuits, antennas, and packaging up to mm-wave frequencies.

Mr. Jamal was a recipient of the 2024 IEEE MTT-S IMS Best Student Paper Award.

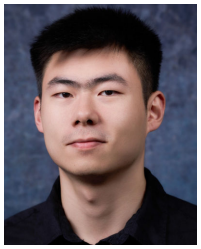

Chenhao Hu (Graduate Student Member, IEEE) received the B.S. degrees in engineering physics and applied mathematics from Emory University, Atlanta, GA, USA, and in electrical engineering from Georgia Institute of Technology, Atlanta, in 2023. He is currently pursuing the M.S. and Ph.D. degrees in electrical and computer engineering at the ATHENA Research Group, Georgia Institute of Technology, under the guidance of Prof. Manos M. Tentzeris.

He is a Research Assistant with Georgia Tech's 3D Systems Packaging Research Center, Atlanta. His current research interests include the design and development of passive RF components and glass/ceramic-based system-on-package for mmWave and sub-THz applications.

Edward Kwao (Graduate Student Member, IEEE) received the B.S. degree in telecommunications engineering from the Kwame Nkrumah University of Science and Technology, Kumasi, Ghana, in 2020, and the M.Eng. degree in intelligence media engineering from Hanbat National University, Daejeon, South Korea, in 2023. He is currently pursuing the Ph.D. degree in electrical and computer engineering at George Mason University, Fairfax, VA, USA.

He is a Research Assistant with the Wireless Cyber Center, George Mason University. His research interests include wireless network security, mmWave communication systems, integrated sensing and communication, RIS and holographic surfaces, and artificial intelligence in wireless communications.

Dr. Kwao received the Best Academic Award from the Graduate School of Software Convergence, Hanbat National University.

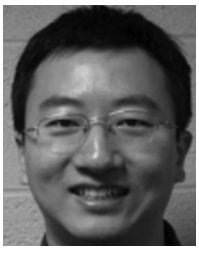

Kai Zeng (Member, IEEE) received the Ph.D. degree in electrical and computer engineering from Worcester Polytechnic Institute (WPI), Worcester, MA, USA, in 2008.

He was a Post-Doctoral Scholar with the Department of Computer Science, University of California at Davis (UCD), Davis, CA, USA, from 2008 to 2011. From 2011 to 2014, he was with the Department of Computer and Information Science, University of Michigan–Dearborn, Dearborn, MI, USA, as an Assistant Professor. He is currently an Associate Professor with the Department of Electrical and Computer Engineering, Cyber Security Engineering and the Department of Computer Science, George Mason University, Fairfax, VA, USA. His current research interests are in cyber–physical system security and privacy, 5G physical layer security, network forensics, and spectrum sharing networks.

Dr. Zeng was a recipient of the U.S. National Science Foundation Faculty Early Career Development (CAREER) Award in 2012, the Excellence in Post-Doctoral Research Award from UCD in 2011, and the Sigma Xi Outstanding Ph.D. Dissertation Award from WPI in 2008. He is an Editor of IEEE TRANSACTIONS ON INFORMATION FORENSICS AND SECURITY, IEEE TRANSACTIONS ON WIRELESS COMMUNICATIONS, and IEEE TRANSACTIONS ON COGNITIVE COMMUNICATIONS AND NETWORKING.

Manos M. Tentzeris (Fellow, IEEE) received the Diploma degree (magna cum laude) in electrical and computer engineering from the National Technical University of Athens, Athens, Greece, and the M.S. and Ph.D. degrees in electrical engineering and computer science from the University of Michigan, Ann Arbor, MI, USA, in 1993 and 1998, respectively.

He was a Visiting Professor with the Technical University of Munich, Munich, Germany, in 2002, GTRI-Ireland, Athlone, Ireland, in 2009, and LAAS-CNRS, Toulouse, France, in 2010, and a Humboldt Guest Professor with FAU, Nuremberg, Germany, in 2019. He is currently the Ed and Pat Joy Chair Professor with the School of Electrical and Computer Engineering, Georgia Institute of Technology, Atlanta, GA, USA, where he heads the ATHENA Research Group (20 researchers). He was the Head of the GT ECE Electromagnetics Technical Interest Group, the Georgia Electronic Design Center Associate Director of RFID/Sensors Research, the Georgia Institute of Technology NSF-Packaging Research Center Associate Director of RF Research, and the RF Alliance Leader. He has helped develop academic programs in 3-D/inkjet-printed RF electronics and modules, fexible electronics, origami and morphing electromagnetics, highly integrated/multilayer packaging for RF, millimeter-wave, sub-THz, and wireless applications using ceramic and organic fexible materials, paper-based RFIDs and sensors, wireless sensors and biosensors, wearable electronics, energy harvesting and wireless power transfer, nanotechnology applications in RF, and SOP-integrated (UWB, multiband, mmW, and conformal) antennas. He has authored more than 850 papers in refereed journals and conference proceedings, seven books, and 26 book chapters.

Dr. Tentzeris is a member of the URSI-Commission D and the MTT-15 Committee, an Associate Member of EuMA, a member of the Technical Chamber of Greece, and a Fellow of the Electromagnetic Academy, He was a recipient/co-recipient of the 2024 IEEE MTT-S IMS Best Student Paper Award, the 2024 Georgia Tech Outstanding Achievement in Research Innovation Award, the 2023 Proceedings of IEEE Best Paper Award, the 2022 Georgia Tech Outstanding Doctoral Thesis Advisor Award, the 2021 IEEE Antennas and Propagation Symposium (APS) Best Student Paper Award, the 2019 Humboldt Research Prize, the 2017 Georgia Institute of Technology Outstanding Achievement in Research Program Development Award, the 2016 Bell Labs Award Competition Third Prize, the 2015 IET Microwaves, Antennas, and Propagation Premium Award, the 2014 Georgia Institute of Technology ECE Distinguished Faculty Achievement Award, the 2014 IEEE RFID-TA Best Student Paper Award, the 2013 IET Microwaves, Antennas and Propagation Premium Award, the 2012 FiDiPro Award in Finland, the iCMG Architecture Award of Excellence, the 2010 IEEE Antennas and Propagation Society Piergiorgio L. E. Uslenghi Letters Prize Paper Award, the 2011 International Workshop on Structural Health Monitoring Best Student Paper Award, the 2010 Georgia Institute of Technology Senior Faculty Outstanding Undergraduate Research Mentor Award, the 2009 IEEE Transactions on Components and Packaging Technologies Best Paper Award, the 2009 E. T. S. Walton Award from the Irish Science Foundation, the 2007 IEEE AP-S Symposium Best Student Paper Award, the 2007 IEEE MTT-S IMS Third Best Student Paper Award, the 2007 ISAP 2007 Poster Presentation Award, the 2006 IEEE MTT-S Outstanding Young Engineer Award, the 2006 Asia-Pacific Microwave Conference Award, the 2004 IEEE Transactions on Advanced Packaging Commendable Paper Award, the 2003 NASA Godfrey "Art" Anzic Collaborative Distinguished Publication Award, the 2003 IBC International Educator of the Year Award, the 2003 IEEE CPMT Outstanding Young Engineer Award, the 2002 International Conference on Microwave and Millimeter-Wave Technology Best Paper Award (Beijing, China), the 2002 Georgia Institute of Technology–ECE Outstanding Junior Faculty Award, the 2001 ACES Conference Best Paper Award, the 2000 NSF CAREER Award, and the 1997 Best Paper Award of the International Hybrid Microelectronics and Packaging Society. He was the General Co-Chair of the 2023 IEEE Wireless Power Transfer Technology Conference and Expo (WPTCE) in San Diego and the 2019 IEEE APS Symposium in Atlanta. He was the TPC Chair of the IEEE MTT-S IMS 2008 Symposium and the Chair of the 2005 IEEE CEM-TD Workshop. He is the Vice-Chair of the RF Technical Committee (TC16) of the IEEE CPMT Society. He is the Founder and the Chair of the RFID Technical Committee (TC24) of the IEEE MTT-S and the Secretary/Treasurer of the IEEE C-RFID. He has served as an Associate Editor for IEEE TRANSACTIONS ON MICROWAVE THEORY AND TECHNIQUES, IEEE TRANSACTIONS ON ADVANCED PACKAGING, and the *International Journal on Antennas and Propagation*. He has given more than 150 invited talks to various universities and companies all over the world. He is currently IEEE EPS Distinguished Lecturer. He has served as one of the IEEE MTT-S Distinguished Microwave Lecturers and as one of the IEEE CRFID Distinguished Lecturers.